

# Molecular simulation of confined ethaline-based deep eutectic solvents for separations of carbon dioxide from methane

Jiaming Xu<sup>1</sup> and Francisco Hung<sup>1</sup>

<sup>1</sup>Northeastern University

December 14, 2022

## Abstract

Classical molecular dynamics simulations were used to study the separation of carbon dioxide from methane by three formulations of the deep eutectic solvent (DES) ethaline (choline chloride: ethylene glycol at 1:2, 1:4 and 1:8 molar ratios), in the bulk and confined inside carbon and titania slit pores of two different pore widths, 2 nm and 5 nm. The highest permselectivities ( $\sim 20$ ) are observed for 1:2 ethaline in a 5 nm carbon pore, followed by the 1:4 DES in a 5 nm graphite pore, 1:2 ethaline in a 2 nm carbon pore and the 1:8 bulk DES. Our results indicate that variations in the ratio of ethylene glycol, which in turn affect the interactions of all DES species with the gas molecules and the different pore walls, plus confinement effects resulting from varying the pore sizes, can affect the gas separation performance of these systems in complex ways.

# Molecular simulation of confined ethaline-based deep eutectic solvents for separations of carbon dioxide from methane

Jiaming Xu and Francisco R. Hung\*

Department of Chemical Engineering, Northeastern University, Boston, MA 02115

## Abstract

Classical molecular dynamics (MD) simulations were used to study the separation of carbon dioxide from methane by three formulations of the deep eutectic solvent (DES) ethaline (choline chloride: ethylene glycol at 1:2, 1:4 and 1:8 molar ratios), confined inside carbon and titania (rutile) slit pores of two different pore widths, 2 nm and 5 nm. In addition, equivalent DES systems in the bulk were studied, which can also be viewed as a model supported DES membrane with  $\mu\text{m}$ -sized pores. Our results indicate that variations in the ratio of ethylene glycol, which in turn affect the interactions of all DES species with the gas molecules and the different pore walls, plus confinement effects resulting from varying the pore sizes, can affect the gas separation performance of these systems in complex ways. The highest permselectivities ( $\sim 20$ ), computed as the product of the diffusivity and solubility selectivities, are observed for 1:2 ethaline in a 5 nm carbon pore, followed by the 1:4 DES in a 5 nm graphite pore, 1:2 ethaline in a 2 nm carbon pore and the 1:8 bulk DES. In bulk systems, all three selectivities reach their highest values for 1:8 ethaline. When the DESs are confined in the nanopores, the solubility selectivity for most systems improves compared to the equivalent bulk systems, with the graphite pores having the largest solubility selectivities for any given ethylene glycol ratio. In contrast, the diffusivity selectivities in confined systems tend to be similar to the values observed in the bulk DESs. Interaction energies and local density profiles were used to rationalize absorption and diffusivity of gases in our systems. Confining ethaline in graphite and rutile nanopores tends to weaken the  $\text{CO}_2$ -ethylene glycol and  $\text{CO}_2$ -cation interactions compared to the values observed in equivalent bulk ethaline systems, which also affect the local density profiles. Our results confirm that variations in ethylene glycol ratio, pore size and pore wall material can lead to significant changes in gas separation performance. Other porous matrices, for example nanoporous polymer formulations and graphene oxides, should be considered in follow-up studies as they may lead to significant improvements in gas separation performance as compared to the bulk DES.

## 1. Introduction

Carbon dioxide capture and storage (CCS) is a suitable approach to reduce the CO<sub>2</sub> load in the atmosphere and achieve carbon neutrality. A main component of CCS is CO<sub>2</sub> separation from gases, including high concentration sources (e.g., natural gas purification plants, refineries) and low concentration sources (e.g., power plants, steel and cement facilities). CO<sub>2</sub> absorption with chemical solvents, typically aqueous amine solutions, is the most widely deployed technology used for carbon dioxide separations, however it requires large amounts of energy to regenerate the solvent. The exceptional intrinsic qualities of ionic liquids (ILs), such as negligible volatility and 'designer-solvent' property tunability, have motivated their study for CO<sub>2</sub> separations (for recent reviews see, e.g., [1-4]). Likewise, deep eutectic solvents (DESs) have also been examined for these separations (see, e.g., [5-10] for recent reviews). DESs have been acknowledged as IL analogs because they share many intrinsic properties and characteristics with ILs [11], plus they tend to be inexpensive, nontoxic and more environmentally friendly than ILs. DESs are typically composed of three species, cations, anions, and hydrogen bond donors (HBDs) to form a eutectic mixture of Lewis or Brønsted acids and bases. However, using ILs and DESs as solvents in gas absorption separations have drawbacks such as elevated cost of some of the ILs and high viscosities, which tend to increase further after CO<sub>2</sub> uptake and lead to mass transfer issues.

One way to overcome the issues above is to incorporate ILs or DESs into materials with nm-sized pores to form supported IL or DES phase materials, or into materials with mm-sized pores to form supported IL or DES membranes. ILs immobilized in porous materials [12-18] and similar DES-based systems [19-23] have been proposed and developed for gas separations, advantages including low energy requirements and low capital and operating costs. For example, experimental results from Craveiro *et al.* [24] showed that CO<sub>2</sub> solubilities range from 0.0055 to 0.006 mol CO<sub>2</sub>/mol DES among different choline chloride-based DES membranes. Lin *et al.* [25] evaluated CO<sub>2</sub> separations by ethaline (choline chloride mixed with ethylene glycol at different molar ratios) immobilized in graphene oxide membranes. Their experimental results show that the capillary force for holding the DES inside the nanoslits can be as high as 90.45 MPa, which is significantly higher than the 0.1 MPa pressure difference used to drive gas flow in their experiments. Moreover, permeance of gases such as CO<sub>2</sub>, H<sub>2</sub>, CH<sub>4</sub> and N<sub>2</sub> decreases, whereas the CO<sub>2</sub> selectivity increases as the molar ratio of ethylene glycol in the DES increases or the membrane thickness decreases. These findings suggest that variables such as pore material, pore width and DES composition can influence the performance of supported DES membranes and phase materials. Molecular simulations are uniquely positioned to fundamentally understand the

effects of these variables on the performance of these complex systems. Our group recently reported classical molecular dynamics (MD) simulations in which we evaluated the uptake of  $\text{CO}_2$  from pure  $\text{CO}_2$  or a binary  $\text{CO}_2$ - $\text{CH}_4$  bulk gas mixture, by a graphite or titania slit pore in which we preadsorbed varying amounts of the ethaline DES (1:2 molar mixture of choline chloride : ethylene glycol), the levuline DES (1:2 molar mixture of choline chloride : levulinic acid), or the IL 1-n-butyl-3-methylimidazolium bis(trifluoromethylsulfonyl)imide,  $[\text{C}_4\text{C}_1\text{im}][\text{Tf}_2\text{N}]$  [26, 27]. Following those reports, here we study the separation of  $\text{CO}_2$  from  $\text{CH}_4$  by three formulations of the ethaline DES (choline chloride : ethylene glycol at 1:2, 1:4 and 1:8 molar ratios), in the bulk and confined in carbon and titania slit pores of two different pore widths, 2 nm and 5 nm. The rest of this article is structured as follows: Section 2 contains computational details, main results are presented and discussed in Section 3 and our concluding remarks are presented in Section 4.

## 2. Computational Models and Methods

Molecular dynamics simulations with the GROMACS software [28] were performed for the DES ethaline confined inside a slit graphite or titania (rutile) pore as well as in bulk systems. Ethaline consists of choline chloride mixed with ethylene glycol, where three different molar ratios were considered, 1:2, 1:4, and 1:8; number of ion pairs and ethylene glycol molecules in our systems are summarized in Table 1. All our confined systems had 180 molecules of  $\text{CO}_2$  and 3420 molecules of  $\text{CH}_4$ , corresponding to a binary gas mixture of 5 mol%  $\text{CO}_2$  and the rest methane, at  $T = 318$  K and bulk pressures of  $P \sim 97$  bar, which are similar to the conditions examined in previous studies of confined ILs and DESs [27, 29]. Bulk simulations had 96 molecules of  $\text{CO}_2$  and 1805 molecules of  $\text{CH}_4$  as adapting different system dimensions without walls. We used a simulation setup (Figure 1) where the DES inside the pore or in the bulk is in contact with two gas reservoirs (connected through periodic boundary conditions) containing the bulk gas mixture. This open-pore configuration simulation setup was shown in our previous studies [26, 27, 30] to lead to proper equilibration of systems of DESs or ILs confined in nanopores and in contact with gases. For example, gas separation results in a confined IL obtained by Budhathoki *et al.* [29] from grand canonical Monte Carlo and MD simulations using a setup where the confined IL is not in direct contact with the bulk gas reservoir, were in good agreement with our results obtained with our open-pore setup shown in Figure 1 [27]. Following our previous studies [26, 27, 30-32], the walls in our graphite nanopores consisted of three graphene layers separated by a gap of 3.35 Å, whereas rutile(110) was used for the walls of our titania nanopores. VMD [33] was used to assemble these pore walls. The surface area of our slit pores was 10.0 and 5.1 nm in the x and y directions. Auxiliary walls, each was modeled as a single graphene layer, were placed to prevent the diffusion of molecules into the vacuum regions on top and bottom of the slit pores in the z-

direction. Our rectangular simulation box had dimensions of 30.0 nm, 5.15 nm and 13.5 nm for confined systems, and 30.0 nm, 10.0 nm and 10.0 nm for bulk systems in the x, y and z directions, with periodic boundary conditions in all three directions (Figure 1).

Table 1. Details of model systems

Molar ratio	Wall material	Pore width (nm)	Number of ion pairs + HBD	Bulk gas pressure at equilibrium (bar)
1:2	graphite	1.97	200 : 400	97.71
1:4	graphite	1.97	140 : 560	97.70
1:8	graphite	1.95	86 : 688	97.65
1:2	graphite	4.98	650 : 1300	97.22
1:4	graphite	5.02	450 : 1800	97.37
1:8	graphite	5.14	280 : 2240	97.31
1:2	rutile	2.00	300 : 600	97.50
1:4	rutile	2.00	200 : 800	97.42
1:8	rutile	2.00	150 : 1200	97.61
1:2	rutile	5.00	740 : 1480	97.21
1:4	rutile	5.00	500 : 2000	97.22
1:8	rutile	5.00	300 : 2400	97.18
1:2	bulk	-	900 : 1800	97.34
1:4	bulk	-	630 : 2520	97.19
1:8	bulk	-	380 : 3040	97.09

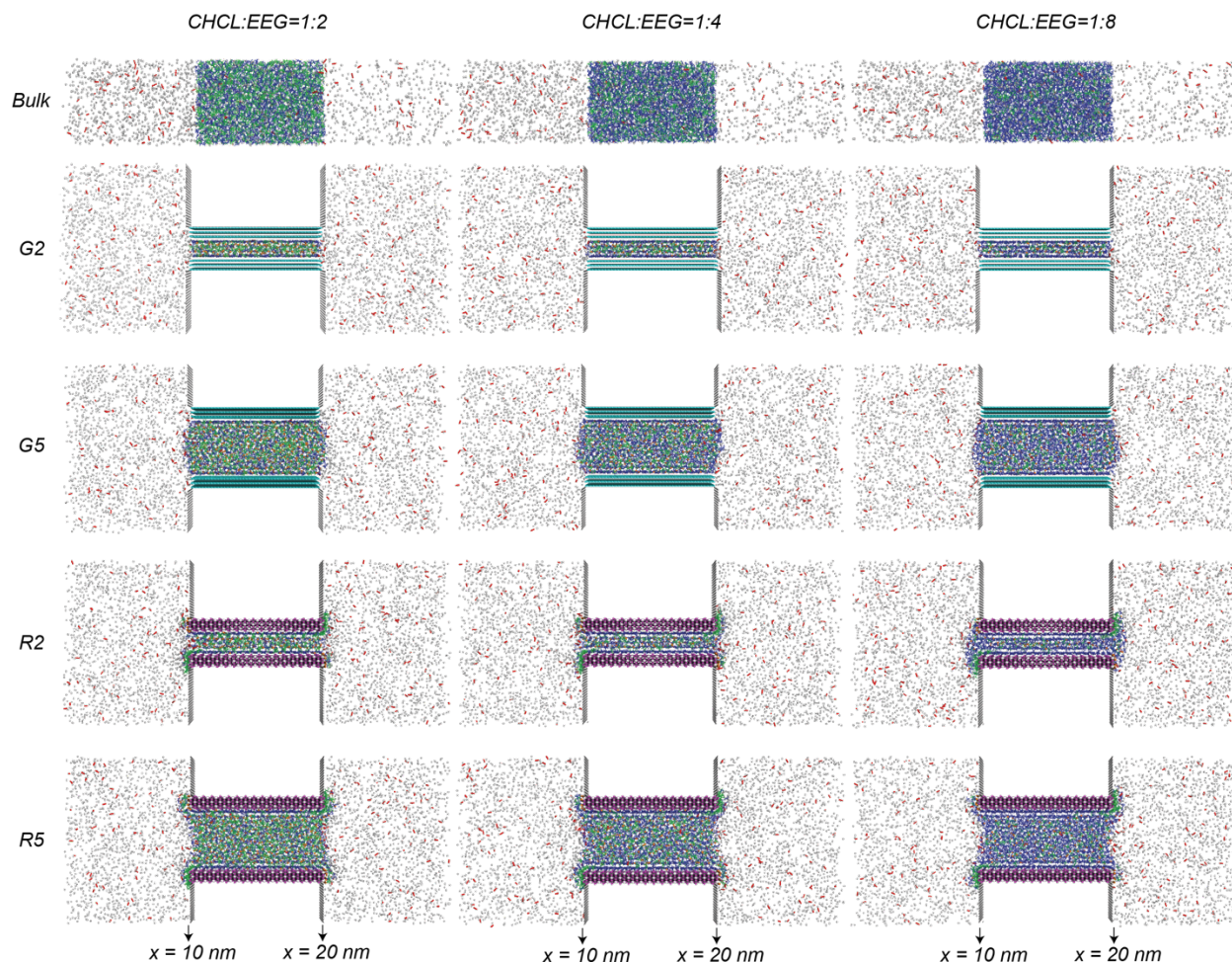


**Figure 1.** Simulation snapshots of ethaline systems at  $T = 318$  K. Molecules are colored as follows: green = choline, orange = chloride, blue = ethylene glycol, red = carbon dioxide, silver = methane. Walls: white = Ti, magenta = O, cyan = carbon, grey = auxiliary walls. Columns from left to right: ethaline with 1:2 molar ratio and 1:4 molar ratio. Rows from top to bottom: bulk, 2 nm graphite, 5 nm graphite, 2 nm titania, and 5 nm titania systems. Bulk-gas interfaces are showed at 10 nm and 20 nm at bottom.

As noted in previous studies [27, 29], the simulated bulk systems can be viewed also as a model supported DES (or IL) membrane with mm-sized pores, whereas our DESs confined in slit nanopores of widths of roughly 2 nm and 5 nm (Table 1) can be viewed as a supported DES phase material with nm-sized pores. Several recent studies have shown that the interactions between a nanoconfined fluid and the pore walls can result in effective pressures inside the pore of up to 20,000 bar [34, 35]. Although it is expected that our open-pore configuration used in our simulation setup (Figure 1) would not allow such extreme pressures to develop inside our pores, for our graphite pores we followed procedures described by recent reports [29, 36], and initially

run NP<sub>zz</sub>T simulations of ethaline inside carbon pores in a closed-pore configuration (where the pore is not connected to the gas reservoirs and periodic boundary conditions are applied to the confined fluid in the x and y directions). These initial simulations were run in LAMMPS [37] for a total of 10 ns. The pressure normal to the graphite walls was set to  $P_{zz} = 1$  bar, the numbers of choline chloride ions and ethylene glycol molecules were fixed, and the pore width was allowed to fluctuate. The purpose of these initial simulations was to obtain configurations where our graphite pores are filled with ethaline with densities comparable to bulk values, the pore widths converge to values close to the targeted 2 nm and 5 nm values (Table 1), and ensure that the pressures of the confined DES inside the pore are not extremely high but on the order of  $P_{zz} \sim 1$  bar. After equilibration, the nanoconfined DES configurations inside graphite pores were put in the open-pore setup in contact with the gas reservoirs and allowed to relax (Figure 1). For our rutile pores, we initially followed the same procedure described above, but when the nanoconfined DESs are put in the open-pore setup, we ended up with rutile pores only partially filled by ethaline as some of the choline chloride ions moved to one of the edges of the rutile walls, while some ethylene glycol molecules moved to the opposite edge. This behavior happens because of the end-wall effects described in our previous studies [26, 27, 30], where one of the wall edges have a large local concentration of O atoms, while the other edge has a larger concentration of Ti atoms. To avoid this situation with our rutile pores, we followed the procedure described in our previous studies [26, 27, 30] where we kept the pore widths fixed at 2 nm and 5 nm, initially placed ethaline species in the side reservoirs and allowed them to diffuse into the pores, as to obtain configurations where the pores are completely filled with ethaline. We monitored the pressures inside the pore and ensured that the confined DES did not develop extremely high pressures before putting the rutile pores in contact with the gas reservoirs. Packmol [38] and PyMOL were used to assemble all initial configurations for ethaline DESs and gas mixtures and system visualizations. Bulk ethaline systems were modeled using elongated orthorhombic simulation boxes (Figure 1), as done in our previous study [27].

As done in our previous studies [26, 27, 30], the general Amber force field (GAFF) was used to model choline chloride and ethylene glycol, with parameters taken from Perkins *et al.* [39], where the partial charges of choline and chloride were set to  $\pm 0.9e$ ; CO<sub>2</sub> and CH<sub>4</sub> were modeled using the TraPPE force field [40, 41]. The carbon atoms in our graphite pores were modeled as Lennard-Jones spheres with parameters  $\sigma_C = 0.340$  nm and  $\epsilon_C = 0.056$  kcal/mol, whereas the titanium and oxygen atoms in the rutile walls were modeled using the Lennard-Jones parameters  $\sigma_{Ti} = 0.392$  nm,  $\epsilon_{Ti} = 0.041$  kcal/mol,  $\sigma_O = 0.303$  nm,  $\epsilon_O = 0.12$  kcal/mol, with partial charges +2.196e and -1.098e for the Ti and O atoms [31, 32, 42, 43]. For simplicity, the graphite and rutile

walls were fixed in space in all our simulations. We have not considered the distortion in the (110) surface of rutile due to hydrogen bonding with oxygen atoms in titania walls. However, previous experimental-simulation studies suggest that this phenomenon was minimized when the surface was in contact with aqueous electrolytic solutions. [44, 45].

Our systems were first subjected to an energy minimization procedure using the steepest descent method, followed by a 5 ns NVT simulation run at 500 K. Each system was then annealed to 318 K over a time of 3 ns, and initially equilibrated for 10 ns before conducting a 190 ns production run. The above steps were repeated for another set of simulations, so that each result presented here are the average of two independent simulation runs for each system examined. The only exceptions were the 1:2 ethaline systems in the bulk and inside 5 nm graphite and rutile pores, which were modeled in our previous study [27] over two independent 100-ns simulation runs. For these systems, the results reported here represent the averages over all our simulation runs, i.e., the two previous trajectories of 100 ns each [27] and two additional runs of 190 ns each. We note that the pore width in our previous study [27] was 5.2 nm, slightly different from the pore widths considered here (Table 1). Nevertheless, the results obtained over the four independent simulation runs were similar to each other. As in our previous simulation studies [26, 27, 30], the improved velocity-rescaling thermostat of Parrinello *et al.* [46] was used to control the temperature, a time step of 1 fs was considered, all bonds with hydrogen atoms were converted to constraints using the LINCS algorithm [47], the nonbonded interaction cutoff was equal to 1.5 nm for both Lennard-Jones and coulombic interactions, and the particle-mesh Ewald (PME) method [48] was applied to calculate long range electrostatic interactions with a grid spacing of 0.1 nm and interpolation order of 6.

By performing these simulations, diffusivity selectivity, solubility selectivity and permselectivity can be evaluated. These variables are defined as follows:

$$\beta_{CO_2,CH_4}^D = \left( \frac{D_{CO_2}}{D_{CH_4}} \right)_{T,P} \quad (1)$$

$$\beta_{CO_2,CH_4}^S = \left( \frac{x_{CO_2}/y_{CO_2}}{x_{CH_4}/y_{CH_4}} \right)_{T,P} \quad (2)$$

$$\beta_{CO_2,CH_4}^\Pi = \frac{\Pi_{CO_2}}{\Pi_{CH_4}} = \beta_{CO_2,CH_4}^S \beta_{CO_2,CH_4}^D \quad (3)$$

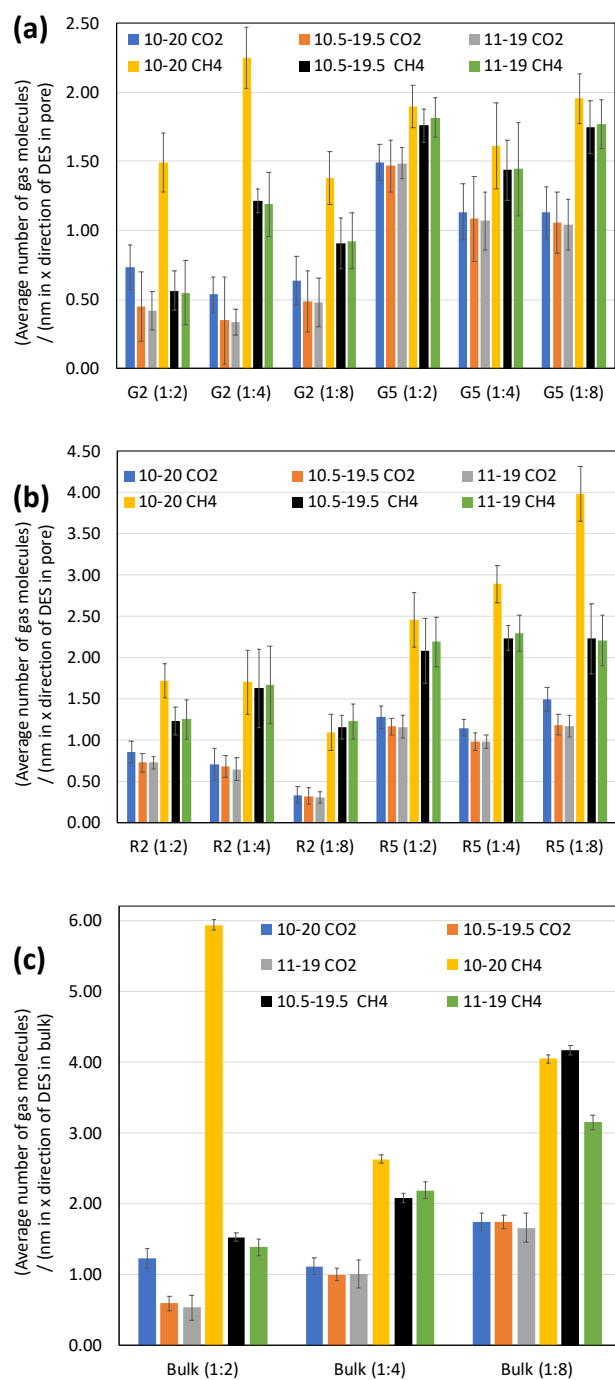
where  $x_i$  and  $y_i$  are the mole fractions of the gas component  $i$  in the liquid or gas phase,  $D_i$  and  $\Pi_i$  are the diffusion coefficient and permeability of the gas component  $i$ , respectively.

### 3. Results and Discussion

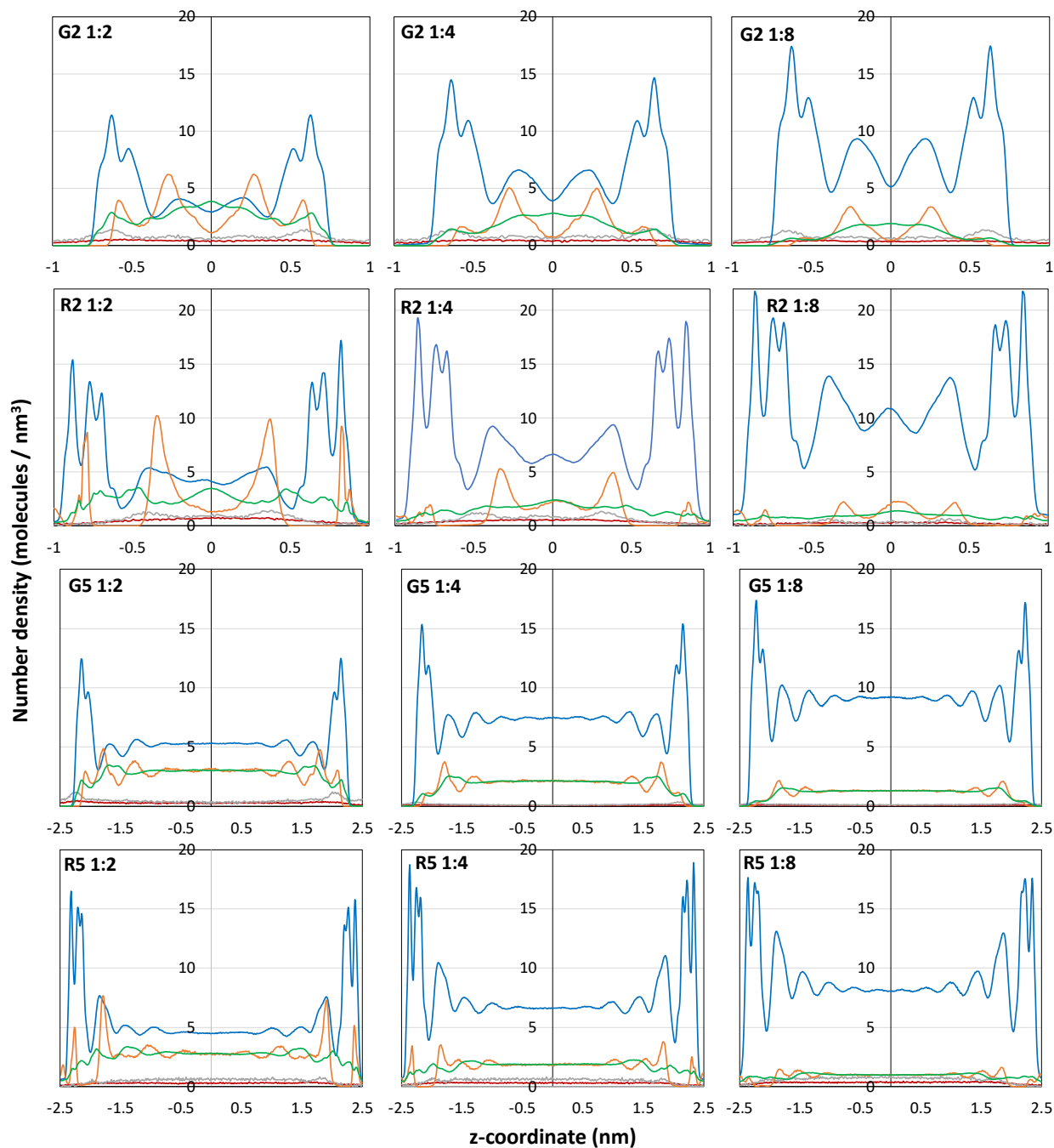
#### 3.1. Gas-DES interfacial effects and local density profiles

Figure 2 shows the number of carbon dioxide and methane molecules absorbed in the DESs in the bulk and inside 2 nm and 5 nm graphite and titania pores, divided by nanometer length of DES in the  $x$  direction (see Figure 1). As reported in previous studies [26, 27, 49], the amounts and compositions of gas absorbed at the gas-DES interface can be significantly different from the values determined in the DES away from the interface.  $\text{CO}_2$  and  $\text{CH}_4$  right at the gas-liquid interface have different local densities and diffusivities compared to the molecules that are in the gas phase or within the liquid DES. These effects are more pronounced in our setup with titania pores as the walls have important end-wall effects, i.e., one edge of the walls has a larger local concentration of O atoms, whereas the other edge has more Ti atoms to keep the whole walls electrically neutral. In consequence, more DES cations will adsorb on one edge of the walls, and more ethylene glycol will adsorb on the other edge, as discussed in our previous studies [26, 27]. As in our simulation setup (Figure 1) any gas molecule with  $x$ -coordinate position ranging between 10-20 nm is in the confined or bulk DES, we analyzed the effect of different cut-off ranges in the  $x$ -coordinate position of the gas molecules in the results shown in Figure 2. We compared the number of  $\text{CO}_2$  and  $\text{CH}_4$  absorbed per nm of DES in the  $x$  direction, as determined using the whole 10-20 nm range, the 10.5-19.5 nm region, and the 11-19 nm range of  $x$ -coordinate values. The number of methane and carbon dioxide molecules per unit length in the liquid phase are the largest when the whole 10-20 nm range is used, but for all systems the gas molecules absorbed per unit length in  $x$  are statistically similar for the 10.5-19.5 and the 11-19 nm ranges. Therefore, all our analyses from now on considered only the gas molecules having  $x$ -coordinate between 10.5-19.5 nm in our systems. We also note that we tracked individual gas molecules in our work, as they could enter and leave the DES phase. The amounts of gas absorbed increase significantly when the gas-DES interface is considered (10-20 nm  $x$ -range), as reported in our previous studies [26, 27]. When comparing increases in gas absorption when the interface is considered against the situation where it is not (10.5-19.5 and 11-19 nm  $x$ -range), the results shown in Figure 2 indicate that the increase in  $\text{CH}_4$  absorbed is larger than the increase in  $\text{CO}_2$  absorbed, again supporting our previous conclusions [26, 27] that interfacial effects do not lead to improvements in  $\text{CO}_2/\text{CH}_4$  solubility selectivity.

From Figure 2, generally all systems exhibit a higher absorption of methane than carbon dioxide in the DESs, which is expected as the bulk gas has 95 mole% of methane. In bulk systems (Figure 2c), the amounts of CO<sub>2</sub> and CH<sub>4</sub> absorbed increase as the ratio of ethylene glycol is raised, however, the trends seem to be system-dependent for the confined DES systems (Figures 2a-b). In the 5 nm rutile pores, the absorption of CO<sub>2</sub> and CH<sub>4</sub> remain statistically similar as the HBD ratio increases, but in the 5 nm graphite pores the amounts of gas absorbed seem to reach minima for 1:4 ethaline, although for CO<sub>2</sub> the results are statistically similar for the 1:4 and 1:8 systems. These observations can be rationalized by analyzing changes in the local structure of these systems, as indicated by local density profiles of all species as a function of the z-direction (Figure 3). In the 5 nm rutile pores no apparent changes are observed in the local density profiles of CO<sub>2</sub> and CH<sub>4</sub> as the HBD ratio is raised. In contrast, in the 5 nm graphite pore increasing the ethylene glycol ratio from 1:2 to 1:4 leads to an increase in its local density near the graphite walls, which causes a reduction in the local density of both gases near the carbon walls; raising the HBD ratio to 1:8 again causes an increase in the local density of this species near the walls, which are already depleted of absorbed gas. In the 2 nm pores, the amount of CH<sub>4</sub> absorbed (Figure 2) has a maximum for 1:4 ethaline confined in both 2 nm graphite and rutile pores. However, the absorption of CO<sub>2</sub> seems to be statistically similar for the three ethylene glycol ratios in 2 nm graphite pores, whereas in 2 nm rutile pores the amount of CO<sub>2</sub> decreases monotonically as the ethylene glycol ratio increases. These observations can again be related to changes in the local structure of the species inside the nanopores. The local density profiles inside both 2 nm pores (Figure 3) indicate that raising the HBD ratio from 1:2 to 1:4 leads to increases in the height of the density peaks of ethylene glycol and to reductions in the peaks of choline and chloride, which in turn causes slight increases in the local densities of CH<sub>4</sub>. Here we note that methane tends to lie close to the pore walls in graphite systems, whereas in rutile pores reductions in local peaks of choline and chloride leads to slight increases in the local density of CH<sub>4</sub> nearby. In the 2 nm graphite pores, no apparent changes in local density are observed for CO<sub>2</sub> (Figure 3), whereas in 2 nm rutile pores the local density of carbon dioxide slightly drops as the HBD ratio increases.



**Figure 2.** Average number of CO<sub>2</sub> and CH<sub>4</sub> molecules per nm of DES in x-direction (a) in graphite pores, (b) in rutile pores, and (c) in bulk. Results in 10.5 - 19.5 nm range were used for all analyses. All relevant data is reported on Table S1 (Supporting Information).



**Figure 3.** Local density profiles along the z-direction of DES species (cation, anion, HBD) and gas molecules ( $\text{CO}_2$ ,  $\text{CH}_4$ ) inside graphite (G) and rutile (R) nanopores of pore widths 2 nm and 5 nm. Colors are same as in Figure 1: green = choline, orange = chloride, blue = ethylene glycol, red = carbon dioxide, silver = methane.

From the local density profiles shown in Figure 8, ethylene glycol has the largest local density close to the graphite or rutile walls in all systems, in agreement with our previous studies

[26, 27, 30]. Increases in the ratio of ethylene glycol in the DES in general lead to increases in the local density of this species near the pore walls and in the center of the pore, and to reductions in the densities of cations, anions and gas molecules. The density peaks of chlorine are usually observed near the density peaks of ethylene glycol for all pore systems. In the carbon pores, the first local density peak of choline is closer to the walls compared to chlorine, with increases in the HBD ratio tending to raise the local density of ethylene glycol near the graphite walls. In the titania pores, changing the HBD ratio from 1:2 to 1:4 also leads to increases in the local density of ethylene glycol near the rutile walls, but as the HBD ratio increases to 1:8 this local density remains relatively unchanged (5 nm pore) or slightly increases (2 nm pore), suggesting that the rutile walls are close to becoming saturated with HBD. This qualitative difference in the adsorption of ethylene glycol on graphite or rutile pores can be explained as ethylene glycol can form strong hydrogen bonds with the rutile walls, whereas it only interacts via weaker van der Waals forces with the graphite walls. As expected, more layering is observed in the 2 nm graphite and rutile pores compared to the 5 nm pores, in which all species have bulk-like behavior in the center regions of the pore. Rutile systems tend to have the strongest layering behavior, which are very pronounced for 1:2 ethaline in a 2 nm titania pore. For most systems, the density peaks for HBD and anions are taller in rutile systems compared to graphite pores, for any given value of HBD ratio and pore size.

### 3.2. Gas diffusion coefficients and diffusivity selectivity

Diffusion coefficients for  $\text{CO}_2$  and  $\text{CH}_4$  absorbed in the confined and bulk DES systems are shown in Figure 4. These diffusion coefficients were calculated from the mean squared displacements (MSDs) in three dimensions. However, as  $\text{CO}_2$  and  $\text{CH}_4$  molecules can enter and leave the DES, individual gas molecules were tracked throughout our production runs, and only the gas molecules absorbed in the DES were considered in our calculations for only the times they remained within the liquid phase. In the bulk DES,  $\text{CO}_2$  and  $\text{CH}_4$  molecules tend to diffuse the fastest in 1:8 ethaline, although the  $\text{CH}_4$  diffusivity in 1:4 ethaline is statistically similar. In most of confined systems, gas molecules tend to diffuse faster as the fraction of ethylene glycol increases from 1:2 to 1:4 and to 1:8, in analogy to our observations for bulk ethaline. The only exception is  $\text{CH}_4$  in a 2 nm graphite pore, where it has the largest diffusivity in 1:4 ethaline; these observations can be linked to the fact that this system has the largest amount of methane absorbed among 2 nm graphite pores (Figure 2), which was rationalized in terms of variations in the local density of species (Figure 3). In general, for any given HBD ratio, both gases tend to diffuse faster in graphite pores compared to rutile pores of the same pore size (Figure 4). The results presented

in Figure 4 also show that gas molecules have smaller diffusivities when they are inside smaller pores (2 nm vs 5 nm), for any given DES ratio (1:2, 1:4 or 1:8) or pore material (graphite or titania).

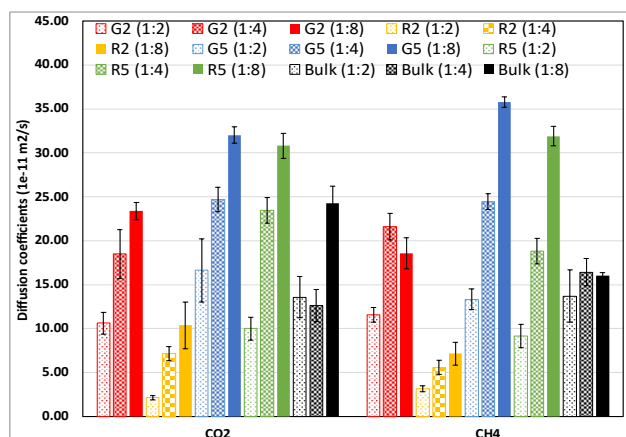


**Figure 4.** Diffusion coefficients of CO<sub>2</sub> and CH<sub>4</sub> in confined and bulk ethaline systems. All relevant data is presented in Table S2 (Supporting Information). Standard errors were used as error bars and they were calculated based on different chunks of MSDs separated by the auto-correlation function, introduced by Grossfield et al [50].

We note that our value of CO<sub>2</sub> diffusivity in bulk 1:2 ethaline,  $(14 \pm 2) \times 10^{-11}$  m<sup>2</sup>/s, is in general agreement with the reported experimental value of  $20.2 \times 10^{-11}$  m<sup>2</sup>/s, as determined by Craveiro *et al.* [24] for the same system, especially as our chosen force fields were not fitted to this specific experimental property. Nevertheless, the comparison also suggests that our chosen models can be improved, especially considering that other non-polarizable force fields have been developed specifically for DESs recently (see, e.g., [51-52]). Comparing the diffusivities of CO<sub>2</sub> and CH<sub>4</sub> in Figure 4 gives a qualitative idea of the diffusivity selectivities in our systems [Equation (1)]. A diffusivity selectivity larger than 1 indicates that CO<sub>2</sub> molecules diffuse through the membrane faster than CH<sub>4</sub>, with larger values desired for industrial processes. CO<sub>2</sub> has smaller diffusivity than CH<sub>4</sub> in bulk 1:2 ethaline (Figure 4), but when the ratio of ethylene glycol is raised to 8, CO<sub>2</sub> has a larger diffusivity than CH<sub>4</sub>. However, in both bulk and confined systems the CO<sub>2</sub> and CH<sub>4</sub> diffusivities tend to have similar magnitude for any given pore material, pore size and HBD ratio, so the diffusivity selectivities are not expected to be very different from 1. Diffusivity selectivities are reported in Figure 5, with relevant data presented in Table S3 (Supporting Information). The largest diffusivity selectivities are observed for 1:8 ethaline in the bulk and 1:8 DES in a 2 nm titania pore, followed closely by 1:8 ethaline in a 2 nm graphite pore, 1:4 DES in a 2 nm rutile pore, 1:2 ethaline in a 5 nm graphite pore and 1:4 DES in a 5 nm rutile pore. In three of our five systems (bulk, 2 nm graphite and rutile systems), increasing HBD ratio leads to

improvements in the diffusivity selectivity, noting however that 1:4 ethaline in the bulk and inside the 2 nm graphite pore has slightly smaller diffusivity selectivity compared to 1:2 and 1:8 ethaline systems. However, in 5 nm graphite pores, increases in the HBD ratio leads to small reductions in diffusivity selectivity, and in 5 nm rutile pores the diffusivity selectivity has a slight maximum for 1:4 ethaline. In most confined systems, the diffusivity selectivity in titania pores seems to be slightly larger than in graphite pores of the same size and with DES of the same HBD ratio, the only exceptions being 1:2 ethaline in 2 nm pores for which the diffusivity selectivity is larger in a graphite pore. In general, Figure 5 suggests that the diffusivity selectivity results seem to be system-dependent, with no particular trends identified. We also note that our measurements have significant uncertainties, mainly caused by the small number of gas molecules present in our systems, especially in the 2 nm pores. Uncertainties in our systems could be reduced by considering larger system sizes and by averaging results over more independent simulation runs, which were not attempted due to the already large computational costs of our study.

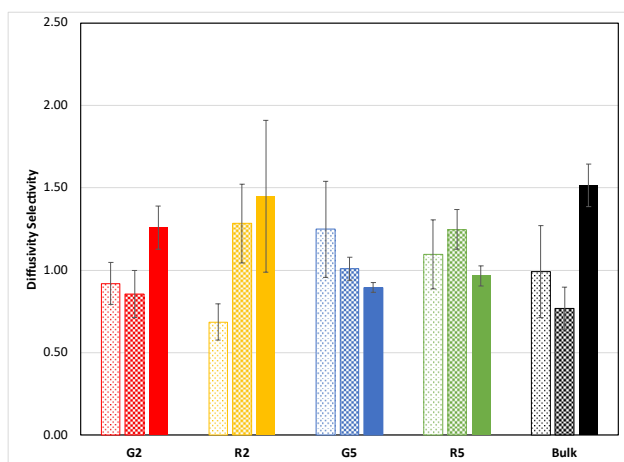


**Figure 5.** CO<sub>2</sub>/CH<sub>4</sub> diffusivity selectivity in ethaline systems. Patterns and colors are same as in Figure 4: 1:2 molar ratio = dotted, 1:4 molar ratio = checkerboard, and 1:8 molar ratio = solid colors. 2 nm graphite and titania nanopores are shown in red and yellow, 5 nm graphite and titania nanopores are shown in blue and green, respectively. All relevant data is reported in Table S3 (Supporting Information)

### 3.3. Interaction energies

As done in our previous studies [26, 27, 30], interaction energies between the different species in our systems can be used to rationalize the diffusivity and selectivity results shown in Figures 4-5. The average interaction energies between different entities in our simulations are shown in Figure 6. In the bulk and carbon pore systems the CO<sub>2</sub>-ethylene glycol and CO<sub>2</sub>-cation

(Figure 6a) are the most dominant interaction energies (i.e., have the largest negative values), however in the smaller 2 nm graphite pore, the ethylene glycol-wall interactions become similar in magnitude to the CO<sub>2</sub>-ethylene glycol and CO<sub>2</sub>-cation energies. In contrast, in the rutile pore systems the HBD-wall and cation-wall are the dominant interactions, especially in the narrower 2 nm titania pore (Figure 6d). In bulk systems, the interaction energies between gas molecules (CO<sub>2</sub> or CH<sub>4</sub>) with both cations and anions decrease in intensity (i.e., become less negative) with increases in the molar ratio of ethylene glycol (Figures 6a-b), whereas the gas-HBD interactions increase in strength (i.e., become more negative) as the ratio of ethylene glycol is raised (Figures 6a-b). The interactions between gas molecules are much weaker in magnitude and remain approximately similar for all bulk systems (Figure 6c). Similar to bulk systems, in all confined systems the gas-cation and gas-anion energies decrease as the HBD ratio is raised, and the CO<sub>2</sub>-HBD interactions increase as the ethylene glycol ratio increases. However, the CH<sub>4</sub>-HBD interactions in all confined systems (Figure 6b) become smaller with increases in the ethylene glycol ratio, which is opposite to the trend described for bulk systems. In all confined systems, the cation-wall energies decrease and the ethylene glycol-wall energies increase as the HBD ratio is raised, whereas the weaker anion-wall energies remain approximately similar. The gas-wall and gas-gas interactions tend to have varying and non-monotonic trends as the HBD ratio increases in confined systems, and in general are weaker in magnitude compared to other interactions present in our systems. For any given pore size and HBD ratio, all interaction energies tend to have larger magnitudes (i.e., are more negative) in rutile systems compared to graphite pores, the exceptions being the CO<sub>2</sub>-cation energy (1:2 system) and the CO<sub>2</sub>-wall energies (all systems) in the 5 nm pores. As reported in our previous studies [26, 27, 30], ethylene glycol and the cation had strong interactions with the pore walls, especially in the case of rutile pores. The Ti and O atoms in rutile have partial charges, and thus can have strong electrostatic interactions and can form hydrogen bonds with ethylene glycol and choline; in contrast, the carbon atoms in our graphite walls have no partial charges and thus interact mainly through dispersion forces with the DES species. The strong wall interactions in rutile pores therefore slow down more the dynamics of DES species near the titania walls, compared to graphite walls.

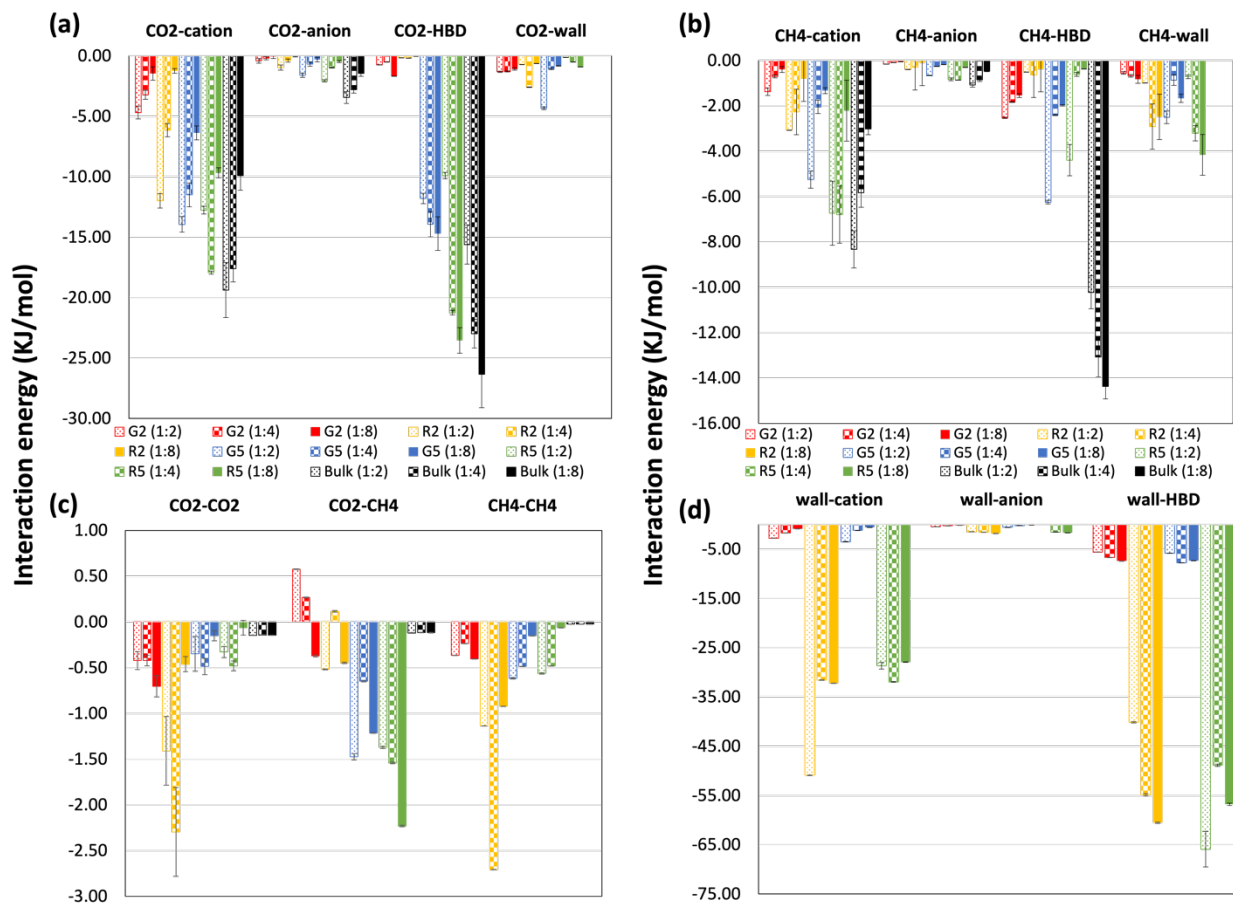


**Figure 6.** Interaction energies between species in our systems. Colors and patterns are same as in Figures 4-5. Energies are reported per mole of CO<sub>2</sub> in (a) and (c), per mole of CH<sub>4</sub> in (b), and per mole of cation, anion or ethylene glycol in (d). All relevant data is reported in Table S4 (Supporting Information)

In Figure 4, the CO<sub>2</sub> and CH<sub>4</sub> diffusivities in confined ethaline tend to increase with increases in the HBD ratio, with the largest gas diffusivities observed for the 1:8 system inside 5 nm graphite and rutile pores. According to the interaction energies shown in Figures 6a-b, these systems have smaller CO<sub>2</sub>-cation, CH<sub>4</sub>-cation and CH<sub>4</sub>-HBD interactions compared to ethaline formulations with lower ratios of ethylene glycol in equivalent 5 nm graphite or rutile pores. The CO<sub>2</sub>-cation, CH<sub>4</sub>-cation and CH<sub>4</sub>-HBD interactions in 1:8 systems inside 5 nm pores are also weaker than the equivalent energies observed in the bulk systems with the same HBD ratio (Figures 6a-b). Increasing the HBD ratio does not lead to large changes in the CO<sub>2</sub>-HBD interactions in the 5 nm graphite pore (Figure 6a), and while in the 5 nm rutile pore these interactions increase as the HBD ratio is raised, the CO<sub>2</sub>-HBD energy determined for the 1:8 system in the rutile pore is still smaller compared to the equivalent energy computed for its bulk

counterpart. As the cation and ethylene glycol interact strongly with the pore walls, especially in rutile systems (Figure 6d), confining ethaline in graphite and rutile nanopores weakens the gas-cation and gas-HBD interactions compared to the values observed in equivalent DES formulations in the bulk. These combined effects seem to lead to increases in the gas diffusivities in confined ethaline as its HBD ratio increases (Figure 4). However, by comparing the sizes of the blue and green bars for CO<sub>2</sub> and CH<sub>4</sub> in Figure 4, we observe that increasing the HBD ratio in the 5 nm pores tends to raise the CH<sub>4</sub> diffusivity slightly more than the diffusion of CO<sub>2</sub>, and thus the selectivity diffusivity (Figure 5) decreases in the 5 nm pores as the HBD ratio is raised. In the 2 nm pores, if we now compare the sizes of the red and yellow bars in Figure 4, CO<sub>2</sub> diffusivities increase faster than CH<sub>4</sub> diffusivities as the HBD ratio is raised, and thus the diffusivity selectivity tends to increase in the 2 nm pores as the ethylene glycol ratio is increased (Figure 5). In this complex interplay we also need to add the confinement effects, in which gas molecules naturally tend to have smaller diffusivities when confined in smaller pores.

### 3.4. Solubility selectivity and permselectivity

Solubility selectivities of CO<sub>2</sub> over CH<sub>4</sub> in our confined DES systems are shown in Figure 7. Solubility selectivity is calculated by Equation (2); a larger value indicates the confined (or bulk) DES tends to preferentially absorb CO<sub>2</sub> over CH<sub>4</sub>, which is what is desired. For all systems, the ratio CO<sub>2</sub>:CH<sub>4</sub> in the DES phase is about 1:1.5, which is far different from the 5:95 ratio initially set for the bulk gas phase. However, we note that in our simulation setup (Figure 1), as CO<sub>2</sub> and CH<sub>4</sub> accumulate in the confined DES phase, the number of molecules in the gas phase decreases and thus both the bulk composition and pressure slightly change from their values at the beginning of the simulation. The largest solubility selectivities (~17) are observed for 1:2 ethaline inside a 5 nm graphite pore, followed by 1:2 ethaline inside a 2 nm graphite pore and 1:4 ethaline in a 5 nm graphite pore, noting however that the solubility selectivities are statistically similar among these three systems. In most systems, the solubility selectivity decreases with increasing molar ratio of ethylene glycol (1:2 > 1:4 > 1:8). The exceptions are the bulk system, in which the solubility selectivity increases when going from 1:2 to 1:4 ethaline and then remains statistically similar for the 1:8 DES, and the 5 nm rutile pore in which the solubility selectivity has a minimum for the 1:4 DES, although again the values are statistically similar. In general, for any given ethaline formulation and pore material, the solubility selectivity slightly increases as the pore sizes increase, the only exception being 1:2 ethaline in rutile pores (although again these values are statistically similar). For any given fixed HBD ratio, confining the DES inside graphite pores tend to slightly increase the solubility selectivity compared to the value observed in the equivalent bulk system. Similarly, the solubility selectivity slightly increases when 1:2 ethaline is

confined in rutile pores compared to the bulk system, however the solubility selectivity of 1:4 ethaline in the bulk is slightly larger than the value of the equivalent system inside rutile pores. In contrast, 1:8 ethaline inside a 5 nm rutile pore has a slightly larger solubility selectivity compared to the 1:8 bulk DES, which in turn has larger selectivity than 1:8 ethaline inside a 2 nm rutile pore. As noted above, changes in local density of the species and their interaction energies can be linked to observed variations in the amounts absorbed and diffusivities of both gases, however linking these changes in local structure and energies to diffusivity and solubility selectivities is not straightforward. Observable selectivities seem to result from a complex interplay between HBD ratio, pore wall material and pore sizes.

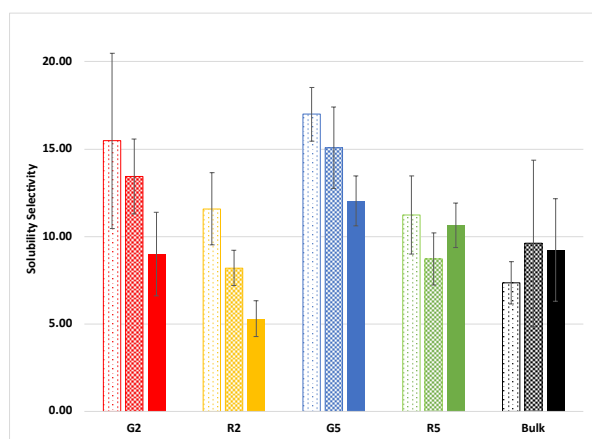


**Figure 7.** CO<sub>2</sub>/CH<sub>4</sub> solubility selectivity in ethaline systems. Patterns and colors are same as in Figures 4-6: 1:2 molar ratio = dotted, 1:4 molar ratio = checkerboard, and 1:8 molar ratio = solid colors. 2 nm graphite and titania nanopores are shown in red and yellow, 5 nm graphite and titania nanopores are shown in blue and green, respectively. All relevant data is presented in Table S3 (Supporting Information).

Permselectivities of CO<sub>2</sub> over CH<sub>4</sub> are shown in Figure 8, which were calculated as the product of the solubility and diffusivity selectivities according to Equation (3). All relevant data are included in Table S3 (Supporting Information). The highest permselectivities (~20) are observed for 1:2 ethaline in a 5 nm carbon pore, followed by the 1:4 DES in a 5 nm graphite pore, 1:2 ethaline in a 2 nm graphite pore and the 1:8 bulk DES, for which all results are statistically similar. In general, for any given HBD ratio and pore size, diffusivity selectivities (Figure 5) tend to be slightly higher in rutile pores compared to graphite slits, the exceptions being the 1:2 DES systems. However, the opposite trend is observed for the solubility selectivities shown in Figure 7, i.e., they are smaller in rutile pores compared to graphite. As a result, the 1:2 ethaline systems have the largest values of permselectivity. In bulk systems, increases in the HBD ratio seem to

lead to increases in permselectivity, but in most of the confined DES increases in the ethylene glycol ratio lead to reductions in permselectivity, except for the 2 nm rutile systems in which the permselectivity seems to reach a local maximum for 1:4 ethaline.

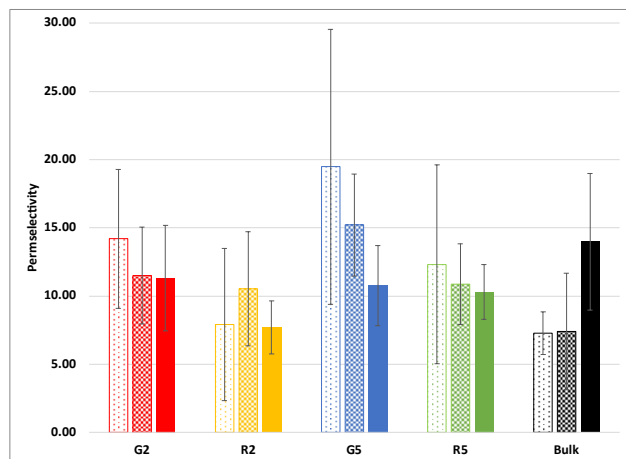


**Figure 8.** CO<sub>2</sub>/CH<sub>4</sub> permselectivity in ethaline systems. Patterns and colors are same as in Figures 4-7: 1:2 molar ratio = dotted, 1:4 molar ratio = checkerboard, and 1:8 molar ratio = solid colors. 2 nm graphite and titania nanopores are shown in red and yellow, 5 nm graphite and titania nanopores are shown in blue and green, respectively. All relevant data is presented in Table S3 (Supporting Information).

As noted in Equation (3), permselectivities can also be calculated as the ratio of the permeabilities of CO<sub>2</sub> and CH<sub>4</sub>, which can be computed from results from our simulations, as explained in our previous study [27]. We did not attempt to calculate gas permeabilities here; however, as discussed in detail in our previous study [27], we found that the permselectivities calculated from gas permeabilities were in general slightly higher than the values determined from the product of the gas solubility and diffusivity selectivities, but both sets of results had similar trends among the systems examined. The computed permselectivity for our 1:2 bulk ethaline system,  $8 \pm 2$ , which was determined at a CO<sub>2</sub> permeability of 63.6 Barrers [27], is in general agreement with the experimental permselectivity ( $\sim 20$  @  $\sim 60$  Barrers, as determined by Craveiro *et al.* [24]). Here we note again that our chosen force fields were not fitted to any experimental data of gases in DES, but again this comparison suggests that other force fields (e.g., [51-52]) should be evaluated for suitability for simulations of gas separations in DESs. As shown by Craveiro *et al.*, permselectivities on the order of  $\sim 100$  can be obtained with bulk 1:2 ethaline, but at CO<sub>2</sub> permeabilities much lower than the values considered here,  $\sim 60$  Barrers. Our results shown in Figure 8 indicate that varying the HBD ratio between 1:2 to 1:8 in ethaline, and varying graphite and rutile pore sizes between 2 and 5 nm, do not seem to lead to dramatic changes in

permselectivity compared to bulk ethaline. However, such a finding was not clear before conducting this study. Our results confirm, however, that variations in HBD ratio, pore size and pore wall material can lead to significant changes in gas separation performance. Therefore, other porous matrices should be considered in follow-up studies, for example nanoporous polymer formulations and graphene oxides [25].

#### 4. Conclusions

The separation of carbon dioxide from methane by three formulations of the ethaline DES (choline chloride : ethylene glycol at 1:2, 1:4 and 1:8 molar ratios), in the bulk and confined inside carbon and titania slit pores of two different pore widths, 2 nm and 5 nm, was studied using classical MD simulations. The bulk systems can be viewed as a model supported DES membrane with  $\mu\text{m}$ -sized pores, whereas the confined systems represent model supported DES phase materials where the DES is immobilized in nm-sized pores. The performance of these systems to treat a bulk gas binary mixture of  $\text{CO}_2$  (5% molar) and  $\text{CH}_4$  at a temperature  $T = 318 \text{ K}$  and a pressure  $P \sim 100 \text{ bar}$  was analyzed in terms of diffusivity selectivity, solubility selectivity and permselectivity. Our results for 1:2 bulk ethaline are in general agreement with recent experimental measurements, especially considering that our models were not fitted to any gas separation data. Our results indicate that variations in the ratio of ethylene glycol, which in turn affect the interactions of all DES species with the gas molecules and the pore walls, plus confinement effects resulting from varying the pore sizes, can affect the gas selectivities in these systems in complex ways. In bulk systems, both the solubility and diffusivity selectivities improve slightly as the HBD ratio is raised to 1:8; as a result, 1:8 ethaline has the largest permselectivity among the bulk systems studied. When the DESs are confined in the nanopores, in general the solubility selectivity slightly increases with respect to the bulk values for any given HBD ratio, and it tends to decrease as the HBD ratio is raised, with the graphite pores showing the largest solubility selectivities among the nanoconfined systems. However, the diffusivity selectivity seems to be affected in more complex ways, with no trends easily identified. Gas molecules tend to diffuse slower in the narrowest pores and tend to have smaller diffusivities in rutile pores compared to graphite pores for any given HBD ratio. As a result, the highest permselectivities ( $\sim 20$ ) are observed for 1:2 ethaline in a 5 nm carbon pore, followed by the 1:4 DES in a 5 nm graphite pore, 1:2 ethaline in a 2 nm graphite pore and the 1:8 bulk DES, for which all results are statistically similar. Interaction energies show that the cation and ethylene glycol interact strongly with the pore walls, especially in rutile systems. Local density profiles suggest that the pore walls tend to become saturated with ethylene glycol as the HBD ratio is raised,

especially the rutile walls, with significant layering effects observed in the narrower pores. Therefore, confining ethaline in graphite and rutile nanopores tends to weaken the gas-cation and gas-HBD interactions compared to the values observed in equivalent ethaline formulations in the bulk, which helps explain why the confined DES have in general larger diffusivity selectivities compared to bulk systems. Whereas variations in the amounts absorbed and diffusivities of both gases can be linked to changes in local density of the species and their interaction energies, linking variations in local densities and energies to changes in selectivities is more complicated. Our results also suggest that our confined systems do not seem to have dramatic permselectivity increases compared to bulk ethaline. Our results confirm, however, that variations in HBD ratio, pore size and pore wall material can lead to significant changes in gas separation performance. Therefore, other porous matrices with oxygenated groups in the walls should be considered in follow-up studies, for example nanoporous polymer formulations and graphene oxides (see, e.g., [25]).

## Acknowledgements

This work was partially supported by the Donors of the American Chemical Society Petroleum Research Fund (grant 58630-ND6). This work used high-performance computational resources from Research Computing at Northeastern University (<https://rc.northeastern.edu>).

## Supporting Information Available

Data reported on Figures 2-7 (Tables S1-S6)

## References

1. Lian, S. H.; Song, C. F.; Liu, Q. L.; Duan, E. H.; Ren, H. W.; Kitamura, Y. Recent advances in ionic liquids-based hybrid processes for CO<sub>2</sub> capture and utilization. *J. Environ. Sci.* **2021**, 99 281-295.
2. Zeng, S. J.; Zhang, X.; Bai, L. P.; Zhang, X. C.; Wang, H.; Wang, J. J.; Bao, D.; Li, M. D.; Liu, X. Y.; Zhang, S. J. Ionic-Liquid-Based CO<sub>2</sub> Capture Systems: Structure, Interaction and Process. *Chem. Rev.* **2017**, 117 (14), 9625-9673.
3. Sheridan, Q. R.; Schneider, W. F.; Maginn, E. J. Role of Molecular Modeling in the Development of CO<sub>2</sub>-Reactive Ionic Liquids. *Chem. Rev.* **2018**, 118 (10), 5242-5260.

4. Zhao, Y.; Dong, Y.; Guo, Y.; Huo, F.; Yan, F.; He, H. Recent progress of green sorbents-based technologies for low concentration CO<sub>2</sub> capture. *Chin. J. Chem. Eng.* **2021**, 31 113-125.
5. Zhang, Y.; Ji, X.; Lu, X. Choline-based deep eutectic solvents for CO<sub>2</sub> separation: Review and thermodynamic analysis. *Renew. Sustain. Energy Rev.* **2018**, 97 436-455.
6. Wagle, D. V.; Adhikari, L.; Baker, G. A. Computational perspectives on structure, dynamics, gas sorption, and bio-interactions in deep eutectic solvents. *Fluid Ph. Equilibria* **2017**, 448 50-58.
7. Hansen, B. B.; Spittle, S.; Chen, B.; Poe, D., et al. Deep Eutectic Solvents: A Review of Fundamentals and Applications. *Chem. Rev.* **2021**, 121 (3), 1232-1285.
8. Atilhan, M.; Aparicio, S. Review and Perspectives for Effective Solutions to Grand Challenges of Energy and Fuels Technologies via Novel Deep Eutectic Solvents. *Energy Fuels* **2021**, 35 (8), 6402-6419.
9. Alkhatib, I. I. I.; Bahamon, D.; Llovel, F.; Abu-Zahra, M. R. M.; Vega, L. F. Perspectives and guidelines on thermodynamic modelling of deep eutectic solvents. *J. Mol. Liq.* **2020**, 298 112183.
10. Rukmani, S. J.; Doherty, B. W.; Acevedo, O.; Colina, C. M. Molecular simulations of deep eutectic solvents: A perspective on structure, dynamics, and physical properties, *Rev. Comput. Chem.* **2022**, 32, 135-216.
11. Smith, E. L.; Abbott, A. P.; Ryder, K. S. Deep eutectic solvents (DESs) and their applications. *Chem. Rev.* **2014**, 114 (21), 11060-11082.
12. Dai, Z. D.; Noble, R. D.; Gin, D. L.; Zhang, X. P.; Deng, L. Y. Combination of ionic liquids with membrane technology: A new approach for CO<sub>2</sub> separation. *J. Membr. Sci.* **2016**, 497 1-20.
13. Tome, L. C.; Marrucho, I. M. Ionic liquid-based materials: a platform to design engineered CO<sub>2</sub> separation membranes. *Chem. Soc. Rev.* **2016**, 45 (10), 2785-2824.
14. Wang, J.; Luo, J.; Feng, S.; Li, H.; Wan, Y.; Zhang, X. Recent development of ionic liquid membranes. *Green Energy Environ.* **2016**, 1 (1), 43-61.
15. Lozano, L.; Godínez, C.; De Los Rios, A.; Hernández-Fernández, F.; Sánchez-Segado, S.; Alguacil, F. J. Recent advances in supported ionic liquid membrane technology. *J. Membr. Sci.* **2011**, 376 (1-2), 1-14.
16. Kohler, F. T.; Popp, S.; Klefer, H.; Eckle, I.; Schrage, C.; Böhringer, B.; Roth, D.; Haumann, M.; Wasserscheid, P. Supported ionic liquid phase (SILP) materials for removal of hazardous gas compounds—efficient and irreversible NH<sub>3</sub> adsorption. *Green Chem.* **2014**, 16 (7), 3560-3568.
17. Klemm, A.; Lee, Y.-Y.; Mao, H.; Gurkan, B. Facilitated transport membranes with ionic liquids for CO<sub>2</sub> separations. *Front. Chem.* **2020**, 8 637.

18. Lee, Y.-Y.; Gurkan, B. Graphene oxide reinforced facilitated transport membrane with poly (ionic liquid) and ionic liquid carriers for CO<sub>2</sub>/N<sub>2</sub> separation. *J. Membr. Sci.* **2021**, 638 119652.
19. Xie, W.; Li, T.; Tiraferri, A.; Drioli, E.; Figoli, A.; Crittenden, J. C.; Liu, B. Toward the Next Generation of Sustainable Membranes from Green Chem. Principles. *ACS Sustain. Chem. Eng.* **2021**, 9 (1), 50-75.
20. Tomé, L. C.; Mecerreyes, D. Emerging Ionic Soft Materials Based on Deep Eutectic Solvents. *J. Phys. Chem. B* **2020**, 124 (39), 8465-8478.
21. Taghizadeh, M.; Taghizadeh, A.; Vatanpour, V.; Ganjali, M. R.; Saeb, M. R. Deep eutectic solvents in membrane science and technology: Fundamental, preparation, application, and future perspective. *Sep. Purif. Technol* **2021**, 258 118015.
22. Wibowo, H.; Susanto, H.; Grisdanurak, N.; Hantoko, D.; Yoshikawa, K.; Qun, H.; Yan, M. Recent developments of deep eutectic solvent as absorbent for CO<sub>2</sub> removal from syngas produced from gasification: Current status, challenges, and further research. *J. Environ. Chem. Eng.* **2021**, 9 (4), 105439.
23. Castro-Muñoz, R.; Galiano, F.; Figoli, A.; Boczkaj, G. Deep eutectic solvents – A new platform in membrane fabrication and membrane-assisted technologies. *J. Environ. Chem. Eng.* **2022**, 10 (2), 106414.
24. Craveiro, R.; Neves, L. A.; Duarte, A. R. C.; Paiva, A. Supported liquid membranes based on deep eutectic solvents for gas separation processes. *Sep. Purif. Technol* **2021**, 254 117593.
25. Lin, H.; Gong, K.; Ying, W.; Chen, D.; Zhang, J.; Yan, Y.; Peng, X. CO<sub>2</sub>-Philic Separation Membrane: Deep Eutectic Solvent Filled Graphene Oxide Nanoslits. *Small* **2019**, 15 (49), 1904145.
26. Shen, Y.; Hung, F. R. A molecular simulation study of carbon dioxide uptake by a deep eutectic solvent confined in slit nanopores. *J. Phys. Chem. C* **2017**, 121 (44), 24562-24575.
27. Shen, Y.; Abedin, R.; Hung, F. R. On the performance of confined deep eutectic solvents and ionic liquids for separations of carbon dioxide from methane: molecular dynamics simulations. *Langmuir* **2019**, 35 (10), 3658-3671.
28. Abraham, M. J.; Murtola, T.; Schulz, R.; Páll, S.; Smith, J. C.; Hess, B.; Lindahl, E. GROMACS: High performance molecular simulations through multi-level parallelism from laptops to supercomputers. *SoftwareX* **2015**, 1-2 19-25.
29. Budhathoki, S.; Shah, J. K.; Maginn, E. J. Molecular simulation study of the performance of supported ionic liquid phase materials for the separation of carbon dioxide from methane and hydrogen. *Ind. Eng. Chem. Res.* **2017**, 56 (23), 6775-6784.
30. Shen, Y.; He, X.; Hung, F. R. Structural and dynamical properties of a deep eutectic solvent confined inside a slit pore. *J. Phys. Chem. C* **2015**, 119 (43), 24489-24500.

31. Rajput, N. N.; Monk, J.; Singh, R.; Hung, F. R. On the influence of pore size and pore loading on structural and dynamical heterogeneities of an ionic liquid confined in a slit nanopore. *J. Phys. Chem. C* **2012**, 116 (8), 5169-5181.
32. Singh, R.; Rajput, N. N.; He, X.; Monk, J.; Hung, F. R. Molecular dynamics simulations of the ionic liquid [EMIM+][TFMSI-] confined inside rutile (110) slit nanopores. *Phys. Chem. Chem. Phys.* **2013**, 15 (38), 16090-16103.
33. Humphrey, W.; Dalke, A.; Schulten, K. VMD: Visual molecular dynamics. *J. Mol. Graph.* **1996**, 14 (1), 33-38.
34. Srivastava, D.; Santiso, E. E.; Gubbins, K. E. Pressure Enhancement in Confined Fluids: Effect of Molecular Shape and Fluid–Wall Interactions. *Langmuir* **2017**, 33 (42), 11231-11245.
35. Gubbins, K. E.; Long, Y.; Śliwinska-Bartkowiak, M. Thermodynamics of confined nanophases. *J. Chem. Thermodyn.* **2014**, 74 169-183.
36. Shao, C.; Ong, W.-L.; Shiomi, J.; McGaughey, A. J. H. Nanoconfinement between Graphene Walls Suppresses the Near-Wall Diffusion of the Ionic Liquid [BMIM][PF6]. *J. Phys. Chem. B* **2021**, 125 (17), 4527-4535.
37. Thompson, A. P.; Aktulga, H. M.; Berger, R.; Bolintineanu, D. S., et al. LAMMPS - a flexible simulation tool for particle-based materials modeling at the atomic, meso, and continuum scales. *Comput. Phys. Commun.* **2022**, 271 108171.
38. Martínez, L.; Andrade, R.; Birgin, E. G.; Martínez, J. M. PACKMOL: A package for building initial configurations for molecular dynamics simulations. *J. Comput. Chem.* **2009**, 30 (13), 2157-2164.
39. Perkins, S. L.; Painter, P.; Colina, C. M. Experimental and computational studies of choline chloride-based deep eutectic solvents. *J. Chem. Eng. Data* **2014**, 59 (11), 3652-3662.
40. Potoff, J. J.; Siepmann, J. I. Vapor–liquid equilibria of mixtures containing alkanes, carbon dioxide, and nitrogen. *AIChE J.* **2001**, 47 (7), 1676-1682.
41. Shi, W.; Maginn, E. J. Atomistic Simulation of the Absorption of Carbon Dioxide and Water in the Ionic Liquid 1-n-Hexyl-3-methylimidazolium Bis (trifluoromethylsulfonyl) imide ([hmim][Tf2N]). *J. Phys. Chem. B* **2008**, 112 (7), 2045-2055.
42. Bandura, A.; Kubicki, J. Derivation of force field parameters for TiO<sub>2</sub>– H<sub>2</sub>O systems from ab initio calculations. *J. Phys. Chem. B* **2003**, 107 (40), 11072-11081.
43. Borodin, O.; Smith, G. D.; Bandyopadhyaya, R.; Bytner, O. Molecular dynamics study of the influence of solid interfaces on poly (ethylene oxide) structure and dynamics. *Macromolecules* **2003**, 36 (20), 7873-7883.
44. Zhang, Z.; Fenter, P.; Cheng, L.; Sturchio, N.; Bedzyk, M.; Předota, M.; Bandura, A.; Kubicki, J.; Lvov, S.; Cummings, P. Ion adsorption at the rutile– water interface: Linking molecular and macroscopic properties. *Langmuir* **2004**, 20 (12), 4954-4969.

45. Předota, M.; Zhang, Z.; Fenter, P.; Wesolowski, D.; Cummings, P. Electric double layer at the rutile (110) surface. 2. Adsorption of ions from molecular dynamics and X-ray experiments. *J. Phys. Chem. B* **2004**, 108 (32), 12061-12072.
46. Bussi, G.; Donadio, D.; Parrinello, M. Canonical sampling through velocity rescaling. *J Chem Phys* **2007**, 126 (1), 014101.
47. Hess, B. P-LINCS: A Parallel Linear Constraint Solver for Molecular Simulation. *J. Chem. Theory Comput.* **2008**, 4 (1), 116-122.
48. Essmann, U.; Perera, L.; Berkowitz, M. L.; Darden, T.; Lee, H.; Pedersen, L. G. A smooth particle mesh Ewald method. *J. Chem. Phys.* **1995**, 103 (19), 8577.
49. Heydari Dokoohaki, M.; Zolghadr, A. R. Significant Improvement in CO<sub>2</sub> Absorption by Deep Eutectic Solvents as Immobilized Sorbents: Computational Analysis. *J. Phys. Chem. B* **2021**, 125 (35), 10035-10046.
50. Grossfield, A.; Patrone, P. N.; Roe, D. R.; Schultz, A. J.; Siderius, D. W.; Zuckerman, D. M. Best practices for quantification of uncertainty and sampling quality in molecular simulations [Article v1. 0]. *Living journal of computational molecular science* **2018**, 1 (1). (<https://doi.org/10.33011/livecoms.1.1.5067>)
51. Zhong, X.; Velez, C.; Acevedo, O. Partial Charges Optimized by Genetic Algorithms for Deep Eutectic Solvent Simulations. *J. Chem. Theory Comput.* **2021**, 17, 3078-3087.
52. Doherty, B.; Acevedo, O. OPLS Force Field for Choline-Chloride-Based Deep Eutectic Solvents. *J. Phys. Chem. B* **2018**, 122, 9982-9993